Supplementary information for

Highly restricted near-surface permafrost extent during the mid-Pliocene warm period

Donglin Guo, Huijun Wang, Vladimir E. Romanovsky, Alan M. Haywood, Nick Pepin, Ulrich Salzmann, Jianqi Sun, Qing Yan, Zhongshi Zhang, Xiangyu Li, Bette L. Otto-Bliesner, Ran Feng, Gerrit Lohmann, Christian Stepanek, Ayako Abe-Ouchi, Wing-Le Chan, W. Richard Peltier, Deepak Chandan, Anna S. von der Heydt, Camille Contoux, Mark A. Chandler, Ning Tan, Qiong Zhang, Stephen J. Hunter, Youichi Kamae

Corresponding author: Donglin Guo (guodl@mail.iap.ac.cn)

This PDF file includes:

1. Figures and tables

   Figure S1 to S14, Table S1 to S3

2. Equation set for the SFI model

3. References from supplementary information

1. Figures and tables

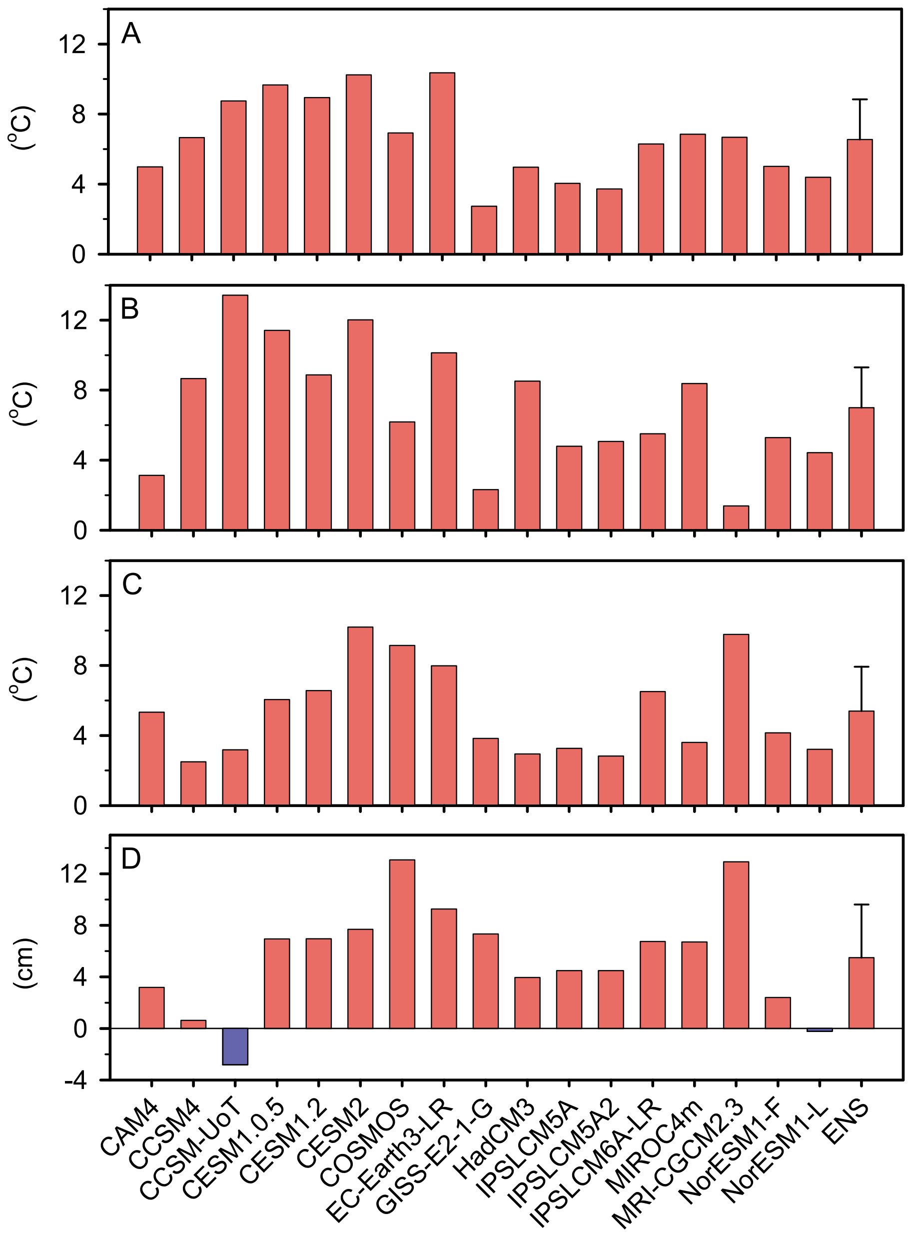

Figure S1. Mean differences in permafrost-relevant climate characteristics between the mid-Pliocene warm period (mPWP) and preindustrial period (PI) (mPWP–PI) averaged over the present-day permafrost region for each PlioMIP2 model and their ensemble (ENS). (A) Mean annual surface air temperature (°C), (B) mean temperature of the warmest month (°C), (C) mean temperature of the coldest month (°C), and (D) mean winter snow depth (cm). The error bar on the ENS bar indicates one standard deviation across the 17 climate models.

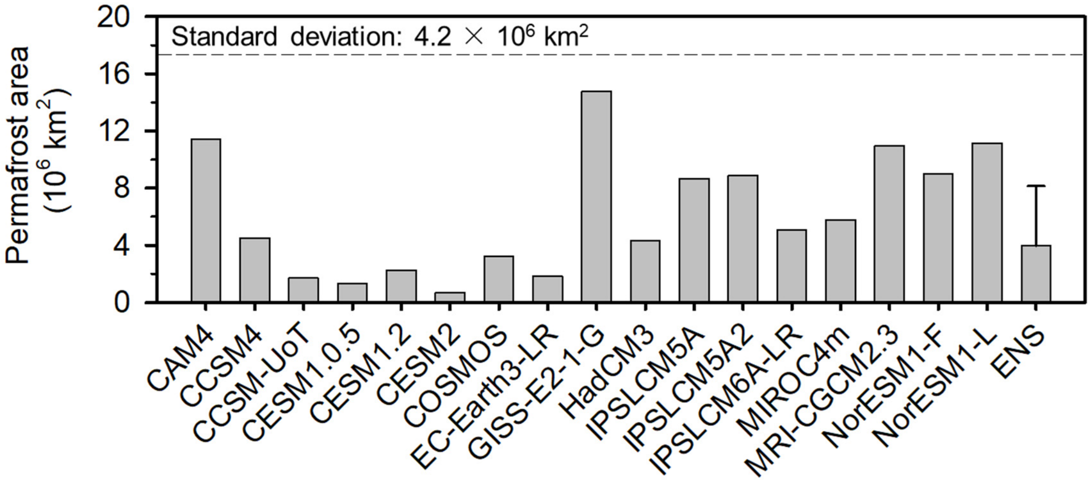

Figure S2. Simulated near-surface permafrost area ($\times 10^6$ km^2) during the mid-Pliocene warm period (mPWP) for each model and the ensemble mean (ENS). The dashed horizontal line represents the permafrost area during the preindustrial period (PI). The error bar on the ENS bar indicates one standard deviation across the 17 climate models.

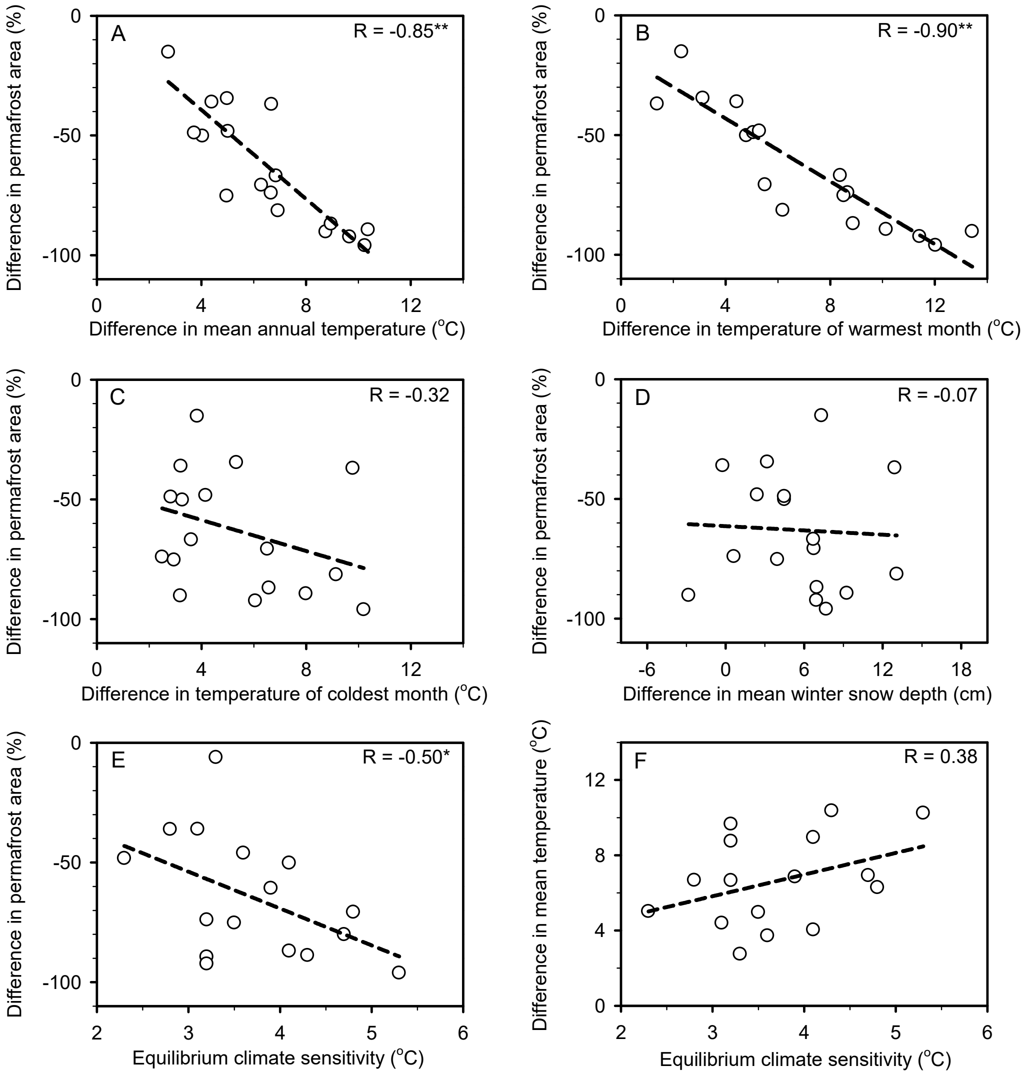

Figure S3. Relationship of simulated difference in near-surface permafrost area between the mid-Pliocene warm period (mPWP) and preindustrial period (PI) (%, (mPWP–PI)/PI×100) with (A) difference in mean annual surface air temperature (mPWP–PI, °C), (B) difference in mean temperature of the warmest month (mPWP–PI, °C), (C) difference in mean temperature of the coldest month (mPWP–PI, °C), (D) difference in mean winter snow depth (mPWP–PI, cm), and (E) equilibrium climate sensitivity (ECS, °C) across the climate models. (F) Relationship of the difference in mean annual surface air temperature between the mPWP and PI (mPWP–PI, °C) with the ECS (°C) across the climate models. All climate variables with respect to temperature and snow are averaged over the present-day permafrost region. The correlation coefficient (R) is given in the top right corner of each panel, with labels "**" ("*") denoting significance at P<0.001 (P<0.05).

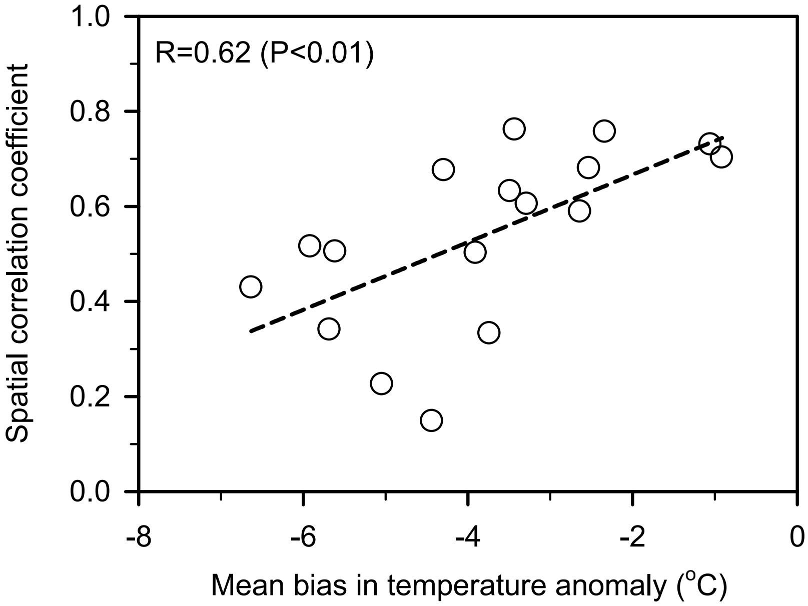

Figure S4. Relationship of mean bias (MB) in simulated and proxy-based temperature anomalies, mid-Pliocene warm period (mPWP) versus preindustrial period (PI) (mPWP–PI, °C) with spatial correlation coefficient in simulated and proxy-based temperature anomalies (mPWP–PI) across the 17 climate models. The correlation coefficient (R) and p value (P) are given in the top left corner of the panel.

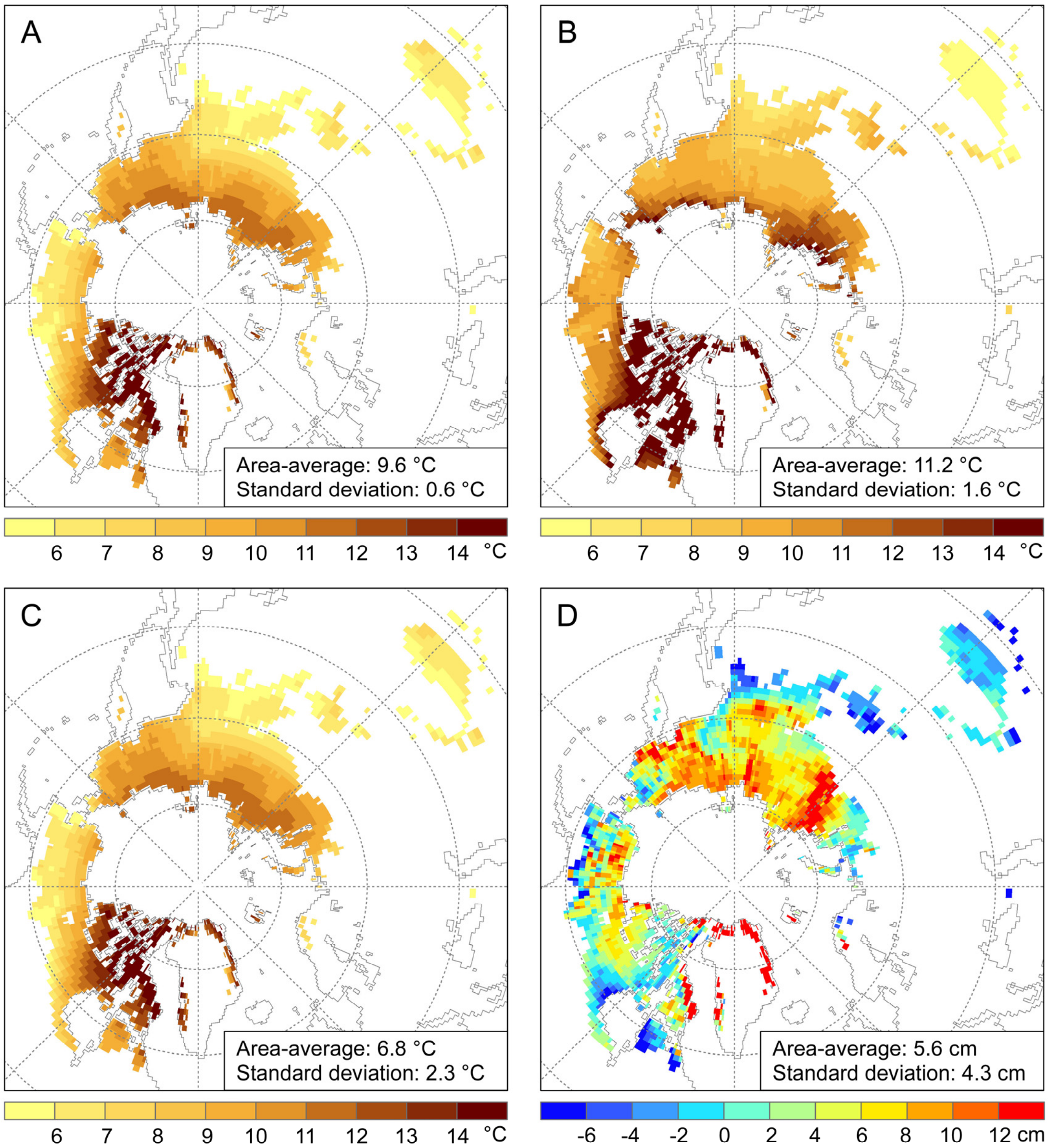

Figure S5. Difference in the model ensemble mean (A) mean annual surface air temperature (°C), (B) mean temperature of the warmest month (°C), (C) mean temperature of the coldest month (°C), and (D) mean winter snow depth (cm) between the mid-Pliocene warm period (mPWP) and preindustrial period (PI) (mPWP–PI) based on the five climate models of model group 1 (–3 °C<MB<0 °C). The area-average over the present-day permafrost region and its standard deviation across the 5 climate models are given in the bottom right of each panel.

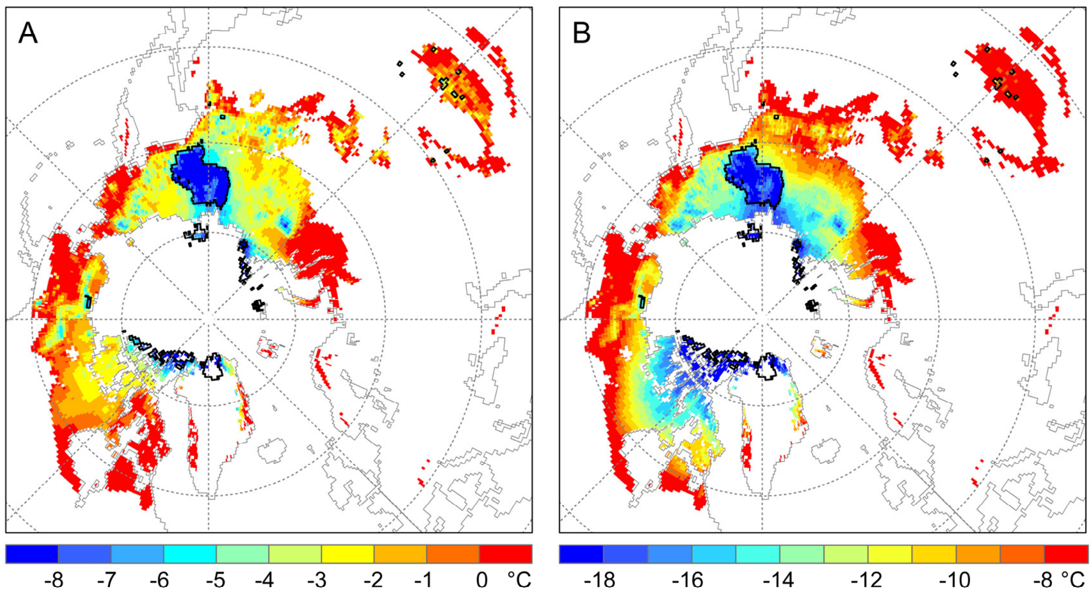

Figure S6. Model ensemble mean (ENS)-corrected annual surface air temperature (°C) during the mid-Pliocene warm period (mPWP) (A) and preindustrial period (PI) (B) based on the five climate models of model group 1 (–3 °C<MB<0 °C). Areas outlined in black refer to the ENS near-surface permafrost extent during the mPWP based on the corrected climate data from model group 1.

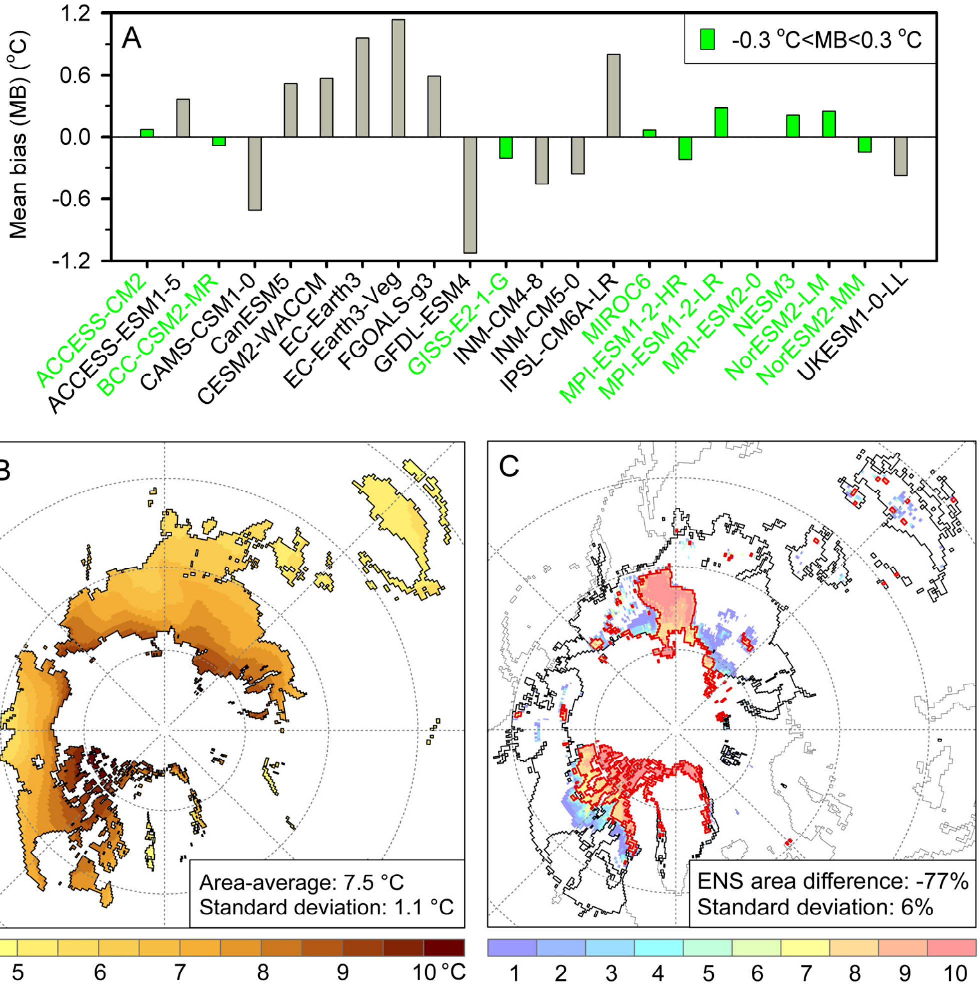

Figure S7. Projected difference in near-surface permafrost extent between 2080–2099 and 1995–2014 under the SSP5-8.5 scenario. (A) Mean bias (MB) of the model-simulated surface air temperature difference between 1901–1930 and 1995–2014 averaged over the present-day permafrost region against CRU observations (simulation minus observation). Green bars represent the 10 preferred models with small MB (–0.3 °C<MB<0.3 °C). (B) Simulated difference in ensemble mean (ENS) surface air temperature from the 10 models with –0.3 °C<MB<0.3 °C between 2080–2099 and 1995–2014 (2080–2099 minus 1995–2014) under the SSP5-8.5 scenario. (C) Simulated difference in ENS near-surface permafrost extent from the 10 models with –0.3 °C<MB<0.3 °C between 2080–2099 (red) and 1995–2014 (black) under the SSP5-8.5 scenario. Shading denotes the differentiation of near-surface permafrost extents during 2080–2099 from the models with –0.3 °C<MB<0.3 °C. The color bar identifies the total number of models that captured near-surface permafrost at a specific location.

ENS area difference is the percentage difference in ENS permafrost area during the period of 2080–2099 relative to 1995–2014. The standard deviation of the difference in the area-averaged surface air temperature and percentage difference in the permafrost area is calculated across the models with –0.3 ℃<MB<0.3 ℃.

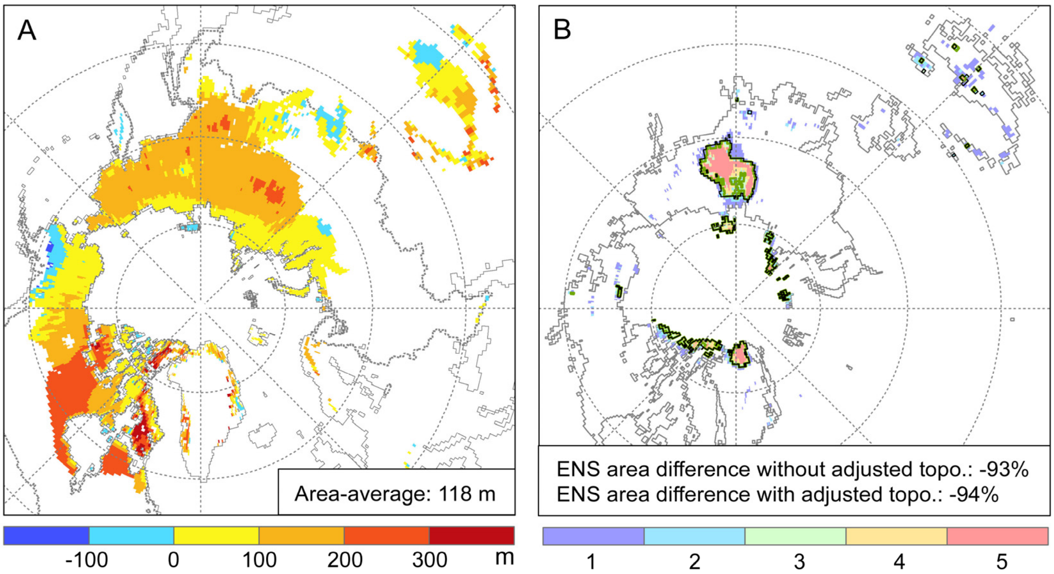

Figure S8. Difference in simulated mid-Pliocene warm period (mPWP) near-surface permafrost extent caused by topographic differences. (A) Difference in PRISM4 topography (m) between mPWP and preindustrial period (PI) (mPWP–PI), with the area-average given in the bottom right of the panel. Positive values indicate higher elevation during the mPWP. (B) Difference in model ensemble mean (ENS) mPWP near-surface permafrost extent based on the 5 climate models of group 1 (–3 °C<MB<0 °C), without adjusted topography (using raw simulated mPWP climate, black) and with adjusted topography (using mPWP climate adjusted to PI topography with the assumed mean atmospheric lapse rate (–0.65 °C/100 m) except for modern ice sheet regions, green). ENS near-surface permafrost extent during the PI is outlined in gray. Shading denotes the differentiation of mPWP near-surface permafrost extent between the 5 models, with adjusted topography. The color bar identifies the total number of models that captured near-surface permafrost in that area. ENS area difference without/with adjusted topography is the percentage difference in ENS near-surface permafrost area during the mPWP relative to the PI.

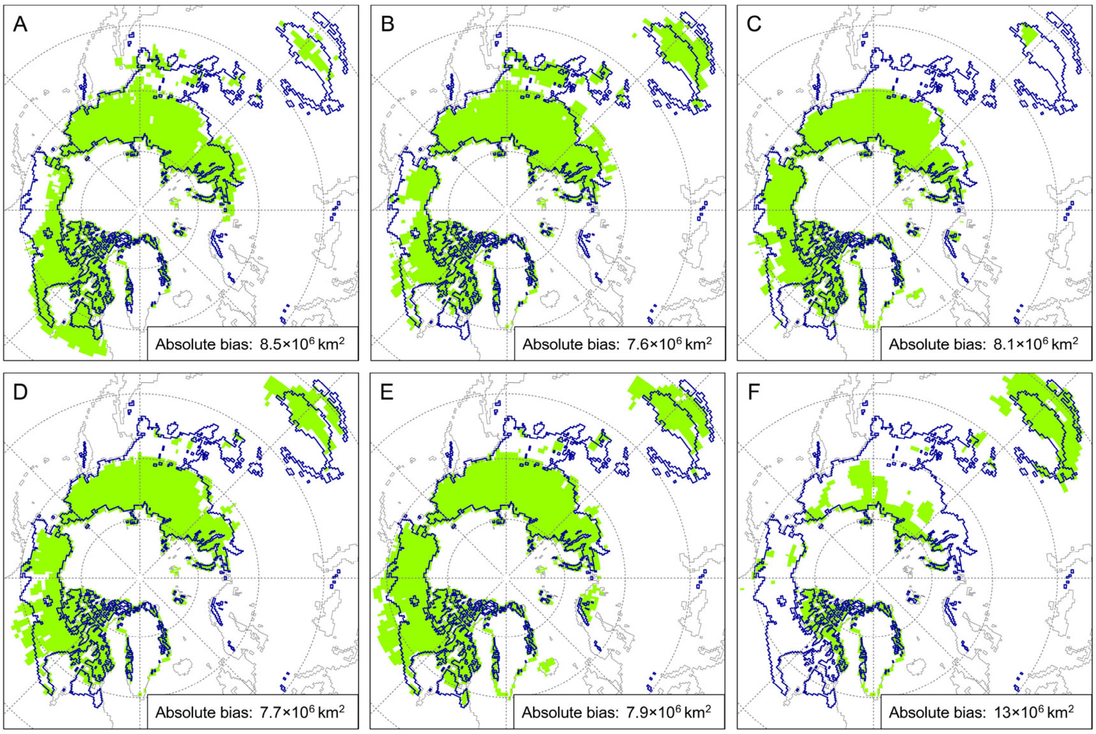

Figure S9. Comparison of simulated preindustrial (PI) near-surface permafrost extent using the raw soil temperature (ST) diagnostic method based on soil temperature at 0–3.5 m depth (green) to the IPA map (areas outlined in blue). (A) CESM2 ST, (B) CESM1.2 ST, (C) CESM1.0.5 ST, (D) CCSM4 ST, (E) CCSM-UoT ST, (F) IPSLCM6A-LR ST. The absolute bias between the simulated area and the IPA map is given in the bottom right corner of each panel.

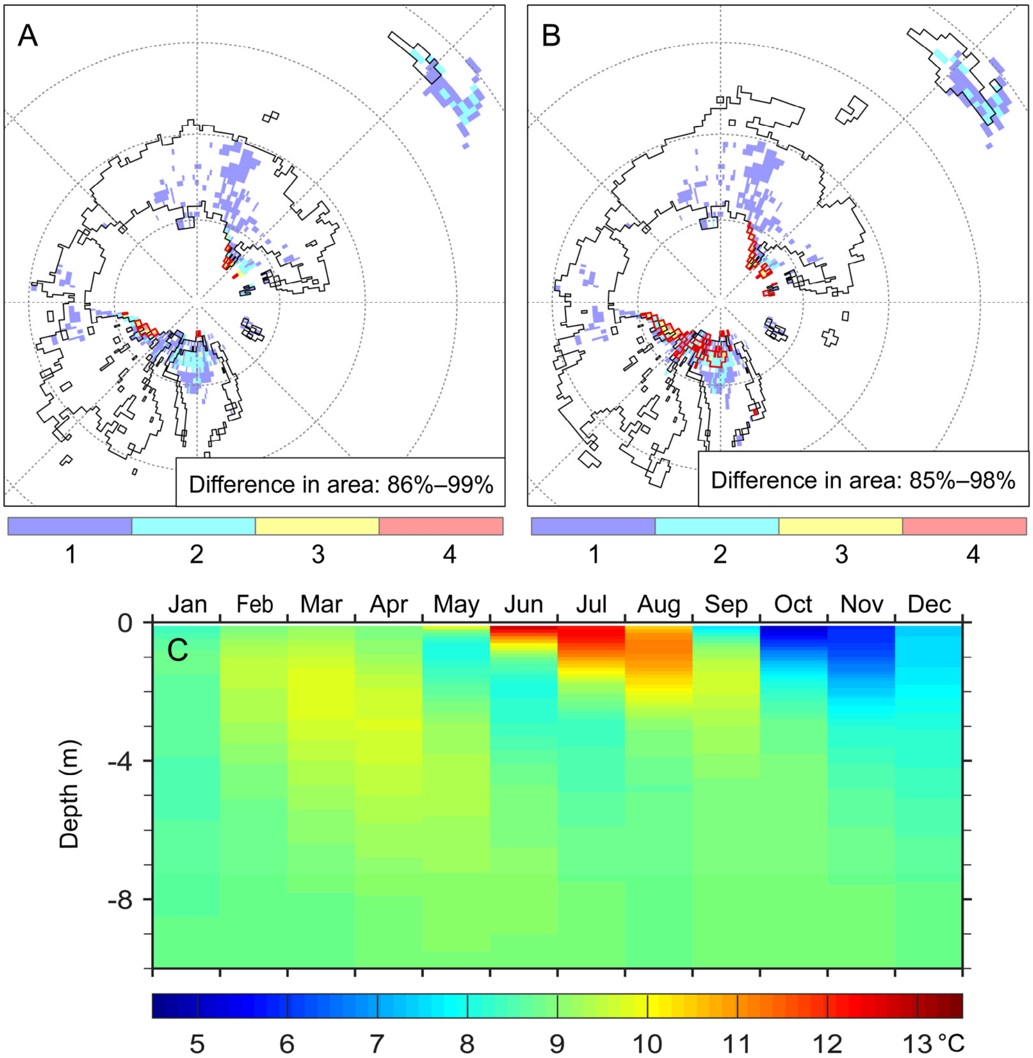

Figure S10. Differences in near-surface permafrost extent between the mid-Pliocene warm period (mPWP) and preindustrial period (PI) diagnosed using soil temperature at 0–3.5 m depth (A) and 0–15 m depth (B) from four climate models (CESM2, CESM1.2, CESM1.0.5, CCSM-UoT) in group 1. (C) Difference in ensemble mean (ENS) soil temperature profile (soil depth-month) (°C) between the mPWP and PI (mPWP–PI) based on the four climate models. In panels (A) and (B), areas outlined in red are the ENS permafrost extent during the mPWP, while areas outlined in black are the respective near-surface permafrost extent during the PI. Shading denotes the differentiation of mPWP permafrost extents from the four models. The unit of each color bar is the total number of models that captured permafrost at that location. The difference in area in panels (A) and (B) is the range of the percentage difference in permafrost area during the mPWP relative to the PI across the four models.

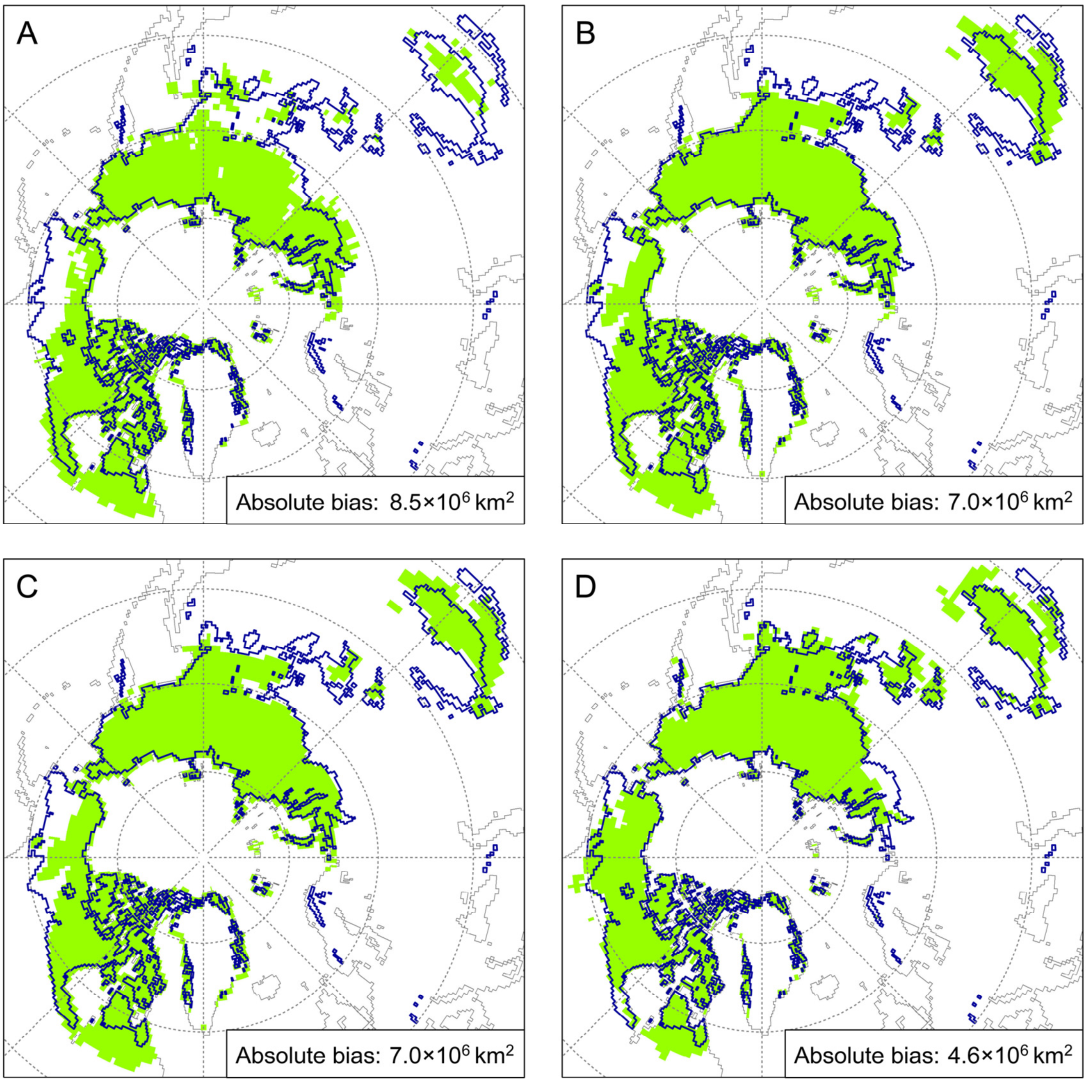

Figure S11. Comparison of different methods of computing the simulated preindustrial (PI) near-surface permafrost extent (green) to the IPA map (areas outlined in blue). (A) raw CESM2 soil temperature (ST) diagnostic method, (B) CESM2 temperature and snow data model SFI method, (C) CESM2 temperature and precipitation (used to calculate snow depth) model SFI method, and (D) coarse resolution CRU temperature and precipitation (used to calculate snow depth) (resampled to CESM grid cells, 0.9° × 1.25°) model SFI method. The resolution of the four simulations is 0.9° × 1.25°. The absolute bias between the simulated area and the IPA map is given in the bottom right corner of each panel.

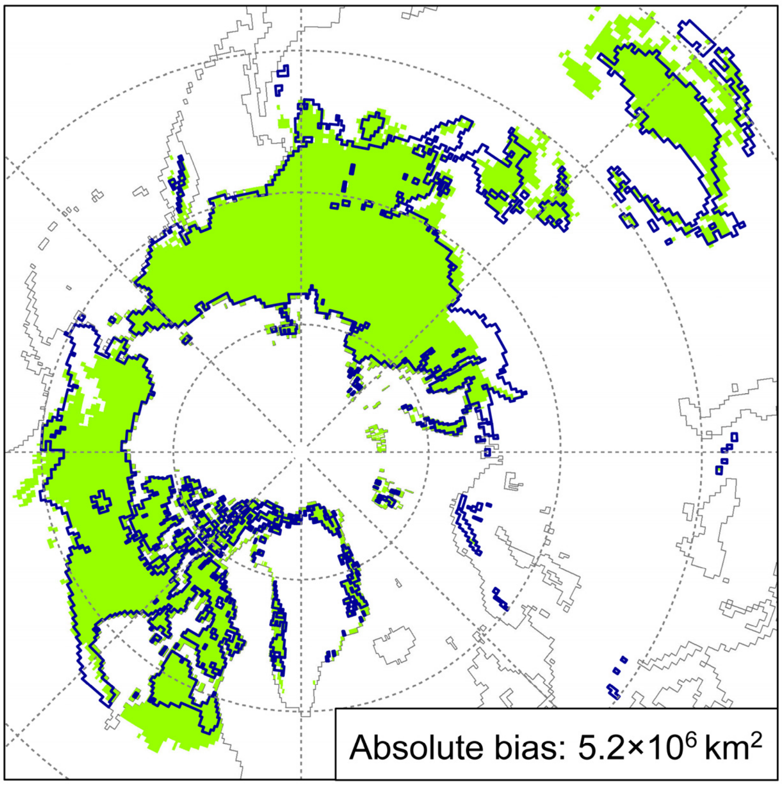

Figure S12. Comparison of simulated preindustrial (PI) near-surface permafrost extent (green) based on high resolution (0.5° × 0.5°) CRU temperature and precipitation (used to calculate snow depth) model SFI method to the IPA map (areas outlined in blue). The resolution of the simulation is 0.5° × 0.5°. The absolute bias between the simulated area and the IPA map is given in the bottom right corner of the panel.

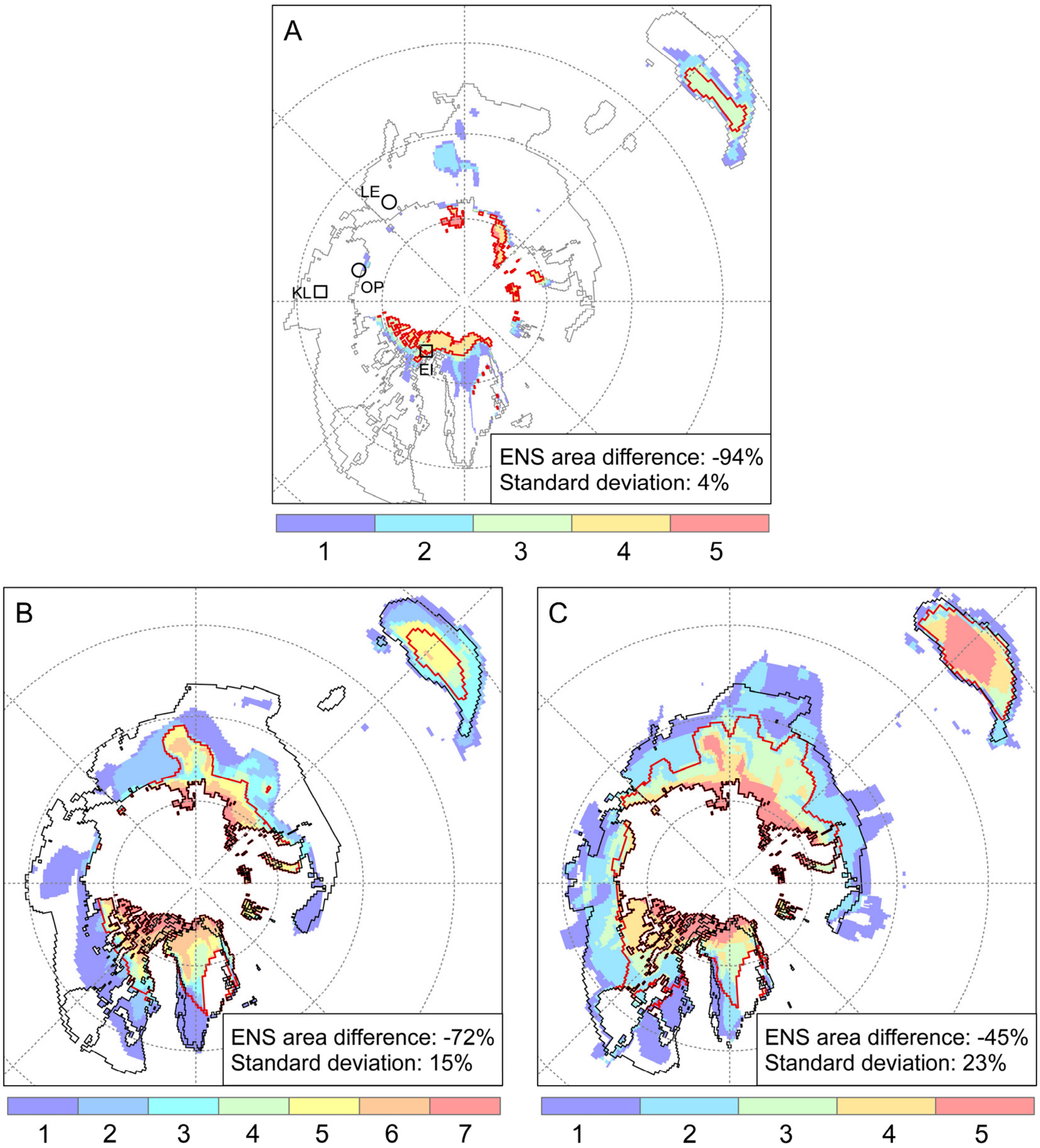

Figure S13. Same as in Figure 3 of the main manuscript, but for results based on raw climate simulation data (i.e., without correction of systematic biases).

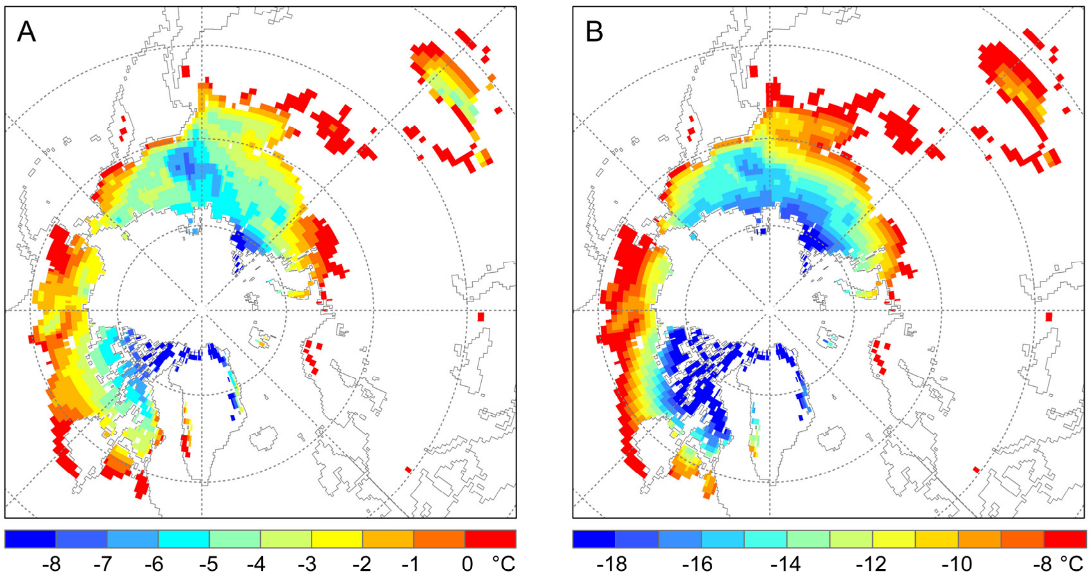

Figure S14. Model ensemble mean raw (without correction of systematic biases) annual surface air temperature (°C) during the mid-Pliocene warm period (mPWP) (A) and preindustrial period (PI) (B) based on the five climate models of model group 1 (–3 °C<MB<0 °C).

Table S1 Details of the 16 PlioMIP2 coupled atmosphere ocean climate models and one atmosphere model, employed for mid-Pliocene warm period (mPWP) permafrost modeling, and basic model-derived statistics.

Model name	Atmosphere resolution (°lon × °lat)	Mean annual temperature difference in present-day permafrost region (mPWP–PI, °C)	Winter snow depth difference in present-day permafrost region (mPWP–PI, cm)	Change in permafrost area from PI to mPWP (%)	Mean bias (MB) in simulated and proxy-based temperature anomalies (mPWP–PI, °C)	Spatial correlation coefficient in simulated and proxy-based temperature anomalies (mPWP–PI)	Equilibrium Climate Sensitivity (ECS, °C) (Haywood et al., 2020)	PlioMIP2 experiment Eoi400 (boundary conditions and experiment citation)
CAM4	0.23 × 0.31	5.0	3.2	–35	–5.9	0.52		Enhanced, 1
CCSM4	0.9 × 1.25	6.7	0.6	–74	–4.3	0.68	3.2	Enhanced, 2
CCSM-UoT	0.9 × 1.25	8.8	–2.8	–90	–2.6	0.59	3.2	Enhanced, 3–5
CESM1.0.5	2.5 × 1.9	9.7	6.9	–92	–2.3	0.76	3.2	Enhanced, 6
CESM1.2	0.9 × 1.25	8.9	7.0	–87	–2.5	0.68	4.1	Enhanced, 2
CESM2	0.9 × 1.25	10.2	7.7	–96	–1.1	0.73	5.3	Enhanced, 2
COSMOS	3.75 × 3.75	6.9	13.1	–81	–3.3	0.61	4.7	Enhanced (dynamic vegetation), 7
EC-Earth3-LR	1.125 × 1.125	10.4	9.3	–89	–0.9	0.70	4.3	Enhanced, 8
GISS-E2-1-G	2.0 × 2.5	2.7	7.3	–15	–6.6	0.43	3.3	Enhanced, 6
HadCM3	3.75 × 2.5	5.0	4.0	–75	–3.7	0.33	3.5	Enhanced, 9
IPSLCM5A	1.9 × 3.75	4.0	4.5	–50	–4.4	0.15	4.1	Enhanced, 10
IPSLCM5A2	1.9 × 3.75	3.7	4.5	–49	–5.0	0.23	3.6	Enhanced, 10
IPSLCM6A-LR	2.5 × 1.26	6.3	6.7	–71	–3.5	0.63	4.8	Enhanced, 11
MIROC4m	2.8 × 2.8	6.9	6.7	–67	–3.4	0.76	3.9	Enhanced, 12
MRI-CGCM2.3	2.8 × 2.8	6.7	12.9	–37	–3.9	0.50	2.8	Standard, 13
NorESM1-F	1.9 × 2.5	5.0	2.4	–48	–5.6	0.51	2.3	Enhanced (modern soils), 14
NorESM-L	3.75 × 3.75	4.4	–0.2	–36	–5.7	0.34	3.1	Enhanced (modern soils) , 14

Table S2 List of proxy sites and their data characteristics during the late Pliocene (modified from Salzmann et al. (2013) (15)).

Location[a]	Continent	Latitude (°)	Longitude (°)	Altitude (masl.)[b]	Age (Ma)	Method[c]	Mean annual temperature (MAT in °C)	Bioclimatic range (°C)[d]	Temporal variability (°C)[e]	Confidence[f]	MAT anomaly (°C)[g]	Reference
Beaver Pond/Ellesmere Isl.	North America	78.4	278	350	3.8–3.4	Multi-Proxies	–1.4	± 4.0	n/a	very high	18.9	16–17
Lena River	Asia	72.20	125.97	5	3.2–2.6	QualEst	1.5	± 1.0	n/a	low	18.8	18
Ocean Point	North America	70	207	308	2.7–2.6	QualEst	1.5	n/a	n/a	medium	11.9	19
Circle, Alaska	North America	65.5	215.92	325	3.6–3.0	QualEst	3.0	n/a	n/a	medium	8.5	20
Blizkiy	Asia	64	162	400	3.6–1.8	CA	5.3	± 5.8	n/a	medium	17.3	21
Nenana Valley, Alaska	North America	64.53	210.92	295	3.6–2.8	QualEst	3.0	n/a	n/a	medium	5.8	20
Lost Chicken Mine	North America	64.06	218.05	325	3.3–2.5	QualEst	2.5	n/a	n/a	medium	9.9	20
Delyankir	Asia	63	133	600	3.3–1.8	CA	7.4	± 0.5	n/a	medium	20.3	21
Magadan District	Asia	59.98	150.65	97	3.2–2.6	QualEst	2.0	n/a	n/a	low	7.1	18
West Siberia	Asia	56.03	70.32	25	3.2–2.6	QualEst	13.5	± 1.5	n/a	low	13.0	22
Merkutlinskiy	Asia	56	72	50	3.3–1.8	CA	11.8	± 4.5	n/a	medium	11.4	21
Kabinet/42 km	Asia	55	80	50	3.3–1.8	CA	8.9	± 2.3	n/a	medium	8.7	21
Mirny	Asia	55	82	50	3.3–1.8	CA	11.2	± 1.3	n/a	medium	10.8	21
Maly-shik/Logovskoy	Asia	54	81	50	3.3–1.8	CA	8.5	± 4.1	n/a	medium	7.8	21
Walton-on-the-Naze**	Europe	51.84	1.27	25	3–2.6	CA[#]	12.8	± 1.3	n/a	high	2.9	23
Willershausen	Europe	51.77	10.10	212	3.2–2.6	CLAMP, CA	13.9	± 2.7	n/a	high	6.2	24
Berga/Thuringia	Europe	51.53	11.02	212	2.65–2.6	CA	13.5	± 0.5	n/a	medium	5.3	24–25
Pula Maar	Europe	47.05	17.38	200	3.0–2.98	CA	12.8	± 1.2	n/a	very high	2.9	26
Oak Grove Forest	North America	45.8	238.4	212	3.05–2.95	CLAMP	11.9	± 1.0	n/a	medium	4.2	27–28
Stirone	Europe	44.6	10.15	779	2.8–2.6	CAM	15	± 2.0	± 3.0	very high	3.7	29
Pavlovskaya Depression	Asia	44.09	132.09	200	3.2–2.6	CA	5.9	± 1.5	n/a	medium	1.6	30
Garraf, Catalonia	Europe	41.17	2.02	62	3.6–3.2	QualEst	19	n/a	n/a	high	4.1	31–32
Kura Depression	Europe	40.53	49.69	226	3.2–2.6	QualEst	21	n/a	n/a	low	6.9	33
California/Sonoma-Napa	North America	38.3	237.55	313	3.45–3.35	CLAMP	17.6	± 2.0	n/a	medium	3.9	28,34
Central Kyushu*	Asia	33.10	131.5	149	2.9–2.8	QuantEst	18.0	n/a	± 1.0	high	3.6	35
Chara Basin, Siberia	Asia	56.97	118.31	700	3.3–3.0	QualEst	12.8	n/a	± 1.8	high	22.0	36
Lake Baikal	Asia	55.69	108.37	450	3.3–3.0	CA[#]	7.0	± 2.5	± 3.0	very high	13.3	37
James Bay Lowland	North America	52.83	276.12	50	3.3–3.0	QualEst	6.0	± 2.0	± 4.0	very high	8.8	38
Lower Rhine Basin	Europe	51.03	6.53	135	3.6–2.6	CLAMP, CA	14.1	± 0.2	± 0.3	very	4.0	39

										high		
Sessenheim-Auenheim	Europe	48.82	8.01	297	3.6–2.6	CA	14.6	± 0.7	± 0.5	high	5.4	40
Alpes-Maritimes	Europe	43.82	7.19	193	3.3–3.2	CAM	17.5	± 2.0	± 0.5	high	5.0	32
Rio Maior	Europe	39.35	351.07	42	3.6–3.0	CAM	16.0	± 2.0	± 2.0	very high	0.5	32
Yorktown, Virginia	North America	36.59	283.62	57	3.5–2.9	QualEst	17.5	n/a	± 0.3	high	2.4	41
Habibas	Africa	35.73	358.88	325	3.6–3.2	CAM	21.0	± 1.0	± 3.0	high	3.2	32,42
Nador	Africa	35.18	357.07	206	3.6–2.6	CAM	21.5	± 1.0	± 3.0	very high	4.4	31

(a) *represents corrected SAT at sea level after Iwauchi (1994) (35); **represents the land surface SAT of the potential nearest terrestrial source area.

(b) Paleoaltitude in units of meters above sea level (masl.), after Sohl et al. (2009) (43) (modern altitude for Delyankir and Chara Basin).

(c) QualEst: qualitative estimates using modern analogs; CLAMP: climate leaf analysis multivariate programme; CAM: climate amplitude method; QuantEst: quantitative estimates using pollen indices; CA: coexistence approach; CA[#]: estimated from Paleoflora Database (44).

(d) Bioclimatic range, in which all taxa of the reconstructed paleovegetation can coexist.

(e) Temporal variability, which indicates the variability in the reconstructed temperature over the time period covered by the fossil record (e.g., orbitally controlled cold and warm cycles).

(d) and (e) n/a represents no range, or climate variability not identified.

(f) For assessing details of confidence, see Salzmann et al. (2013) (15).

(g) The mean annual temperature anomaly is calculated as the individual site mean annual temperature record minus the nearest grid cell-mean CRU temperature during 1901–1930.

Table S3 Details of the 22 Climate Model Intercomparison Project phase 6 climate models, employed for present day and future permafrost modelling, and basic model-derived statistics. The models are divided into two groups: (1) –3 °C<MB<3 °C and (2) MB<–3 °C or MB> 3 °C. In addition to the results from individual models, we provide the ensemble mean of each group.

Model name	Resolution (°lon ×°lat)	Mean bias (MB) in simulated and CRU temperature anomalies in present-day permafrost region (1995–2014 minus 1901–1930, °C)	Mean annual temperature difference in present-day permafrost region (2080–2099 minus 1995–2014, °C, SSP5-8.5)	Change in permafrost area from 1995–2014 to 2080–2099 (%, SSP5-8.5)	Model reference
Model group 1:					
ACCESS-CM2	1.25 × 1.88	0.07	8.9	−86	45
BCC-CSM2-MR	1.13 × 1.13	−0.08	7.3	−82	47
GISS-E2-1-G	2.0 × 2.5	−0.20	7.3	−86	54
MIROC6	1.41 × 1.41	0.07	8.3	−82	58
MPI-ESM1-2-HR	0.96 × 0.96	−0.22	6.4	−69	59
MPI-ESM1-2-LR	1.88 × 1.88	0.28	6.5	−71	60
MRI-ESM2-0	1.13 × 1.13	0.0	6.7	−80	61
NESM3	1.88 × 1.88	0.21	9.6	−93	62
NorESM2-LM	1.88 × 2.5	0.25	6.7	−81	63
NorESM2-MM	0.94 × 1.25	−0.15	7.0	−77	63
Ensemble mean		0.02±0.17	7.5±1.1	−77±6	
Model group 2:					
ACCESS-ESM1-5	1.24 × 1.88	0.36	7.4	−79	46
CAMS-CSM1-0	1.13 × 1.13	−0.71	4.3	−47	48
CanESM5	2.81 × 2.81	0.52	11.8	−96	49
CESM2-WACCM	0.94 × 1.25	0.57	8.9	−90	50
EC-Earth3	0.70 × 0.70	0.96	9.6	−89	51
EC-Earth3-Veg	0.70 × 0.70	1.14	9.4	−85	51
FGOALS-g3	2.25 × 2.0	0.59	6.0	−62	52
GFDL-ESM4	1.0 × 1.25	−1.13	6.0	−69	53
INM-CM4-8	1.5 × 2.0	−0.46	5.1	−62	55
INM-CM5-0	1.5 × 2.0	−0.36	5.4	−61	56
IPSL-CM6A-LR	1.26 × 2.5	0.80	10.9	−95	57
UKESM1-0-LL	1.25 × 1.88	−0.37	13.3	−97	64
Ensemble mean		0.16±0.70	8.2±2.8	−85±16	

2. Equation set for the SFI model (65)

For the surface without snow:

$$\bar{T} = (\overline{T_h} + \overline{T_c})/2 \quad (1)$$

$$A = (\overline{T_h} - \overline{T_c})/2 \quad (2)$$

$$\beta = \cos^{-1}(-\bar{T}/A) \quad (3)$$

$$\overline{T_s} = \bar{T} + A(\sin\beta/\beta) \quad (4)$$

$$\overline{T_w} = \bar{T} - A[\sin\beta/(\pi - \beta)] \quad (5)$$

$$L_s = 365(\beta/\pi) \quad (6)$$

$$L_w = 365 - L_s \quad (7)$$

$$DDT = \overline{T_s} \times L_s \quad (8)$$

$$DDF = -\overline{T_w} \times L_w \quad (9)$$

$$\mathrm{SFI} = \frac{\sqrt{DDF}}{\sqrt{DDF}+\sqrt{DDT}} \quad (10)$$

where $\bar{T}$ is the mean annual air temperature (°C), A is the annual temperature amplitude (°C), $\overline{T_h}$ and $\overline{T_c}$ are the mean temperatures (°C) of the warmest and coldest months, respectively, β is the "frost angle", that is the point along the time axis where the temperature curve crosses a threshold of 0 °C, $\overline{T_s}$ and $\overline{T_w}$ are the mean summer and winter temperatures (°C), respectively, L_s and L_w are the length of summer and winter (days), respectively, DDT is the sum of thawing degree days, and DDF is the sum of freezing degree days.

For the surface with snow:

$$\bar{T} = (\overline{T_h} + \overline{T_c})/2 \quad (11)$$

$$A = (\overline{T_h} - \overline{T_c})/2 \quad (12)$$

$$\beta = \cos^{-1}(-\bar{T}/A) \quad (13)$$

$$\overline{T_s} = \bar{T} + A(\sin\beta/\beta) \quad (14)$$

$$\overline{T_w} = \bar{T} - A(\sin\beta/(\pi - \beta)) \quad (15)$$

$$L_s = 365(\beta/\pi) \quad (16)$$

$$L_w = 365 - L_s \quad (17)$$

$$DDT = \overline{T_s} \times L_s \quad (18)$$

$$Z_{*s} = (\propto_s P/\pi)^{1/2} \quad (19)$$

$$\propto_s = \lambda_s/(c_s \times \rho_s) \quad (20)$$

$$\lambda_s = 2.1 \times 10^{-2} + 4.2 \times 10^{-4}\rho_s + 2.2 \times 10^{-9}{\rho_s}^3 \quad (21)$$

$$c_s = 7.79 \times \overline{T_w} + 2115 \quad (22)$$

$$A_* = A \exp(-\overline{Z_s}/Z_{*s}) \quad (23)$$

$$\overline{T_{w*}} = \bar{T} - A_*(\sin\beta/(\pi - \beta)) \quad (24)$$

$$DDF^* = -\overline{T_{w*}} \times L_w \quad (25)$$

$$\text{SFI} = \frac{\sqrt{DDF^*}}{\sqrt{DDF^*} + \sqrt{DDT}} \quad (26)$$

where Z_{*s} is the damping depth (m) in the snow, P is the length of the annual temperature cycle (s), $\propto_s$ is the thermal diffusivity of snow (m^2 s^{-1}), λ_s is the thermal conductivity of snow (W m^{-1} °C^{-1}), ρ_s is the density of snow (kg m^{-3}), c_s is the specific heat capacity of snow (J kg^{-1} °C^{-1}), A_* is the temperature amplitude at the surface with snow (°C), $\overline{Z_s}$ is the mean winter snow depth (m), $\overline{T_{w*}}$ is the mean winter temperature (°C) incorporating snow effects, and DDF^* is the sum of freezing degree days incorporating snow effects.

3. References from supplementary information

1. Q. Yan *et al.*, Enhanced intensity of global tropical cyclones during the Mid-Pliocene warm period. *Proc. Nat. Acad. Sci.* **113**, 12963–12967 (2016).
2. R. Feng, B. Otto-Bliesner, E. Brady, N. Rosenbloom, Increased climate response and earth system sensitivity from CCSM4 to CESM2 in Mid-Pliocene simulations. *J. Adv. Model. Earth Sys.* **12**, e2019MS002033 (2020).
3. W. Peltier, G. Vettoretti, Dansgaard-Oeschger oscillations predicted in a comprehensive model of glacial climate: A “kicked” salt oscillator in the Atlantic. *Geophys. Res. Lett.* **41**, 7306–7313 (2014).
4. D. Chandan, W. Peltier, Regional and global climate for the mid-Pliocene using the University of Toronto version of CCSM4 and PlioMIP2 boundary conditions. *Clim. Past* **13**, 919–942 (2017).
5. D. Chandan, W. Peltier, On the mechanisms of warming the mid-Pliocene and the inference of a hierarchy of climate sensitivities with relevance to the understanding of climate futures. *Clim. Past* **14**, 825–856 (2018).
6. A. Haywood *et al.*, The Pliocene Model Intercomparison Project Phase 2: large-scale climate features and climate sensitivity. *Clim. Past* **16**, 2095–2123 (2020).
7. C. Stepanek, E. Samakinwa, G. Knorr, G. Lohmann, Contribution of the coupled atmosphere–ocean–sea ice–vegetation model COSMOS to the PlioMIP2. *Clim. Past* **16**, 2275–2323 (2020).

8. Q. Zhang *et al.*, Simulating the mid-Holocene, last interglacial and mid-Pliocene climate with EC-Earth3-LR. *Geosci. Model Dev.* **14**, 1147–1169 (2021).
9. S. Hunter, A. Haywood, A. Dolan, J. Tindall, The HadCM3 contribution to PlioMIP phase 2. *Clim. Past* **15**, 1691–1713 (2019).
10. N. Tan *et al.*, Modeling a modern-like pCO_2 warm period (Marine Isotope Stage KM5c) with two versions of an Institut Pierre Simon Laplace atmosphere–ocean coupled general circulation model. *Clim. Past* **16**, 1–16 (2020).
11. T. Lurton *et al.*, Implementation of the CMIP6 forcing data in the IPSL-CM6ALR model. *J. Adv. Model. Earth Sys.* **12**, e2019MS001940 (2020).
12. W. Chan, A. Abe-Ouchi, Pliocene Model Intercomparison Project (PlioMIP2) simulations using the Model for Interdisciplinary Research on Climate (MIROC4m). *Clim. Past* **16**, 1523–1545 (2020).
13. Y. Kamae, K. Yoshida, H. Ueda, Sensitivity of Pliocene climate simulations in MRI-CGCM2.3 to respective boundary conditions. *Clim. Past* **12**, 1619–1634 (2016).
14. X. Li, C. Guo, Z. Zhang, O. Otterå, R. Zhang, PlioMIP2 simulations with NorESM-L and NorESM1-F. *Clim. Past* **16**, 183–197 (2020).
15. U. Salzmann *et al.*, Challenges in quantifying Pliocene terrestrial warming revealed by data–model discord. *Nat. Clim. Change* **3**, 969–974 (2013).
16. N. Rybczynski *et al.*, Mid-Pliocene warm-period deposits in the High Arctic yield insight into camel evolution. *Nat. Commun.* **4**, 1550 (2013).
17. A. Ballantyne *et al.*, Significantly warmer Arctic surface temperatures during the

Pliocene indicated by multiple independent proxies. *Geology* **38**, 603–606 (2010).

18. A. Fradkina, in Abstracts of the Joint US/USSR Workshop on Pliocene Paleoclimates. (eds. Thompson, R.S., Borisova, O.K. & Svetlitskaya, T.V.), pp. 22 (1991).
19. R. Nelson, L. Carter, Pollen analysis of a late Pliocene & early Pleistocene section from the Gubik Formation of Arctic Alaska. *Quaternary Res.* **24**, 295–306 (1985).
20. T. Ager, J. Matthews, W. Yeend, Pliocene terrace gravels of the ancestral Yukon River near Circle, Alaska: Palynology, paleobotany, paleoenvironmental reconstruction and regional correlation. *Quatern. Int.* **22–23**, 185–206 (1994).
21. S. Popova, T. Utescher, D. Gromyko, A. Bruch, V. Mosbrugger, Palaeoclimate Evolution in Siberia and the Russian Far East from the Oligocene to Pliocene – Evidence from Fruit and Seed Floras. *Turkish J. Earth Sci.* **21**, 315–334 (2012).
22. V. Volkova, in Abstracts of the Joint US/USSR Workshop on Pliocene Paleoclimates. (eds. Thompson, R.S., Borisova, O.K. & Svetlitskaya, T.V.), pp. 44–45 (1991).
23. M. Head, Pollen and dinoflagellates from the Red Crag at Walton-on-the-Naze, Essex; evidence for a mild climatic phase during the early late Pliocene of eastern England. *Geol. Mag.* **135**, 803–817 (1998).
24. D. Uhl *et al.*, Cenozoic paleotemperatures and leaf physiognomy: A European perspective. *Palaeogeogr. Palaeoclimatol. Palaeoecol.* **248**, 24–31 (2007).
25. D. Mai, H. Walther, Die pliozänen Floren von Thüringen, Deutsche Demokratische Republik. *Quartärpaläontology* **7**, 55–297 (1988).

26. K. Willis, A. Kleczkowski, S. Crowhurst, 124,000-year periodicity in terrestrial vegetation change during the late Pliocene epoch. *Nature* **397**, 685–688 (1999).

27. J. Wolfe, in Pliocene Climates: Scenario for Global Warming. (eds. Gosnell, L.B. & Poore, R.Z.), 39–42 (1990).

28. R. Thompson, Pliocene environments and climates in the western United States. *Quaternary Sci. Rev.* **10**, 115–132 (1991).

29. S. Fauquette, A. Bertini, Quantification of the northern Italy Pliocene climate from pollen data: evidence for a very peculiar climate pattern. *Historical Biol.* **32**, 361–369 (2003).

30. N. Blokhina, O. Bondarenko, Woody plant assemblages and palaeoenvironments in the Pliocene of Pavlovskaya Depression (Southern Primory'e). *Acta Palaeontol. Rom.* **4**, 23–35 (2004).

31. S. Fauquette *et al.*, Climate and biomes in the West Mediterranean area during the Pliocene. *Palaeogeogr. Palaeoclimatol. Palaeoecol.* **152**, 15–36 (1999).

32. J. Suc, J. Cravatte, Etude palynologique du Pliocene de Catalogne (Nord-ouest de l'Espagne). *Paléobiologie continentale* **13**, 1–31 (1982).

33. A. Mamedov, in Abstracts of the Joint US/USSR Workshop on Pliocene Paleoclimates. (eds. Thompson, R.S., Borisova, O.K. & Svetlitskaya, T.V.), pp. 28–31 (1991).

34. D. Axelrod, The Sonoma Flora (California). Publ. Carnegie Inst. Wash. 553, 167–206 (1944).

35. A. Iwauchi, Late Cenozoic vegetational and climatic changes in Kyushu, Japan.

Palaeogeogr. Palaeoclimatol. Palaeoecol. **108**, 229–280 (1994).

36. F. Enikeev, The Late Cenozoic of northern Transbaikalia and paleoclimates of southern East Siberia. *Russ. Geol. Geophys.* **49**, 602–610 (2008).
37. D. Demske, B. Mohr, H. Oberhansli, Late Pliocene vegetation and climate of the Lake Baikal region, southern East Siberia, reconstructed from palynological data. *Palaeogeogr. Palaeoclimatol. Palaeoecol.* **184**, 107–129 (2002).
38. C. Gao *et al.*, Glaciation of North America in the James Bay Lowland, Canada, 3.5 Ma. *Geology* **40**, 75–978 (2012).
39. T. Utescher, V. Mosbrugger, A. Ashraf, Terrestrial Climate Evolution in Northwest Germany over the Last 25 Million Years. *Palaios* **15**, 430–449 (2000).
40. V. Teodoridis, Z. Kvaček, D. Uhl, Late Neogene palaeoenvironment and correlation of the Sessenheim-Auenheim floral complex. *Palaeodiversity* **2**, 1–17 (2009).
41. D. Willard, Palynological record from the North Atlantic region at 3 Ma: vegetational distribution during a period of global warmth. *Rev. Palaeobot. Palyno.* **83**, 275–297 (1994).
42. J. Suc *et al.*, Zanclean (~Brunssumian) to early Piacenzian (~ early-middle Reuverian) climate from 4 to 54 north latitude (West Africa, West Europe and West Mediterranean areas). *Meded. Rijks Geol. Dienst.* **52**, 43–56 (1995).
43. L. Sohl *et al.*, PRISM3/GISS topographic reconstruction. U. S. Geol. Surv. Data Series 419, 6 pp. (2009).
44. T. Utescher, V. Mosbrugger, Palaeoflora Database. Available at

http://www.palaeoflora.de (2010).

45. D. Bi *et al.*, Configuration and spin-up of ACCESS-CM2, the new generation Australian Community Climate and Earth System Simulator Coupled Model. *J. South. Hemisph. Earth Syst. Sci.* **70**, 225–251 (2020).

46. T. Wu *et al.*, The Beijing Climate Center Climate System Model (BCC-CSM): the main progress from CMIP5 to CMIP6. *Geosci. Model Dev.* **12**, 1573–1600 (2019).

47. M. Kelley *et al.*, GISS-E2.1: Configurations and climatology. *J. Adv. Model. Earth Syst.* **12**, e2019MS002025 (2020).

48. H. Tatebe *et al.*, Description and basic evaluation of simulated mean state, internal variability, and climate sensitivity in MIROC6. *Geosci. Model Dev.* **12**, 2727–2765 (2019).

49. W. Müller *et al.*, A higher-resolution version of the Max Planck Institute Earth System Model (MPI-ESM1.2-HR). *J. Adv. Model. Earth Syst.* **10**, 1383–1413 (2018).

50. T. Mauritsen *et al.*, Developments in the MPI-M Earth System Model version 1.2 (MPI-ESM1.2) and its response to increasing CO_2. *J. Adv. Model. Earth Syst.* **11**, 998–1038 (2019).

51. S. Yukimoto *et al.*, The MRI Earth System Model version 2.0, MRI-ESM2.0: description and basic evaluation of the physical component. *J. Meteorol. Soc. Jpn.* **97**, 931–965 (2019).

52. J. Cao *et al.*, The NUIST Earth System Model (NESM) version 3: Description and preliminary evaluation. *Geosci. Model Develop.* **11**, 2975−2993 (2018).

53. Ø. Seland *et al.*, Overview of the Norwegian Earth System Model (NorESM2) and key climate response of CMIP6 DECK, historical, and scenario simulations. *Geosci. Model Dev.* **13**, 6165–6200 (2020).

54. T. Ziehn *et al.*, The Australian Earth System Model: ACCESS-ESM1.5. *J. South. Hemisph. Earth Syst. Sci.* **70**, 193–214 (2020).

55. X. Rong *et al.*, The CAMS climate system model and a basic evaluation of its climatology and climate variability simulation. *J. Meteorol. Res.* **32**, 839–861 (2018).

56. N. Swart *et al.*, The Canadian Earth System Model version 5 (CanESM5.0.3). *Geosci. Model Dev.* **12**, 4823–4873 (2019).

57. P. Lauritzen *et al.*, NCAR release of CAM-SE in CESM2. 0: A reformulation of the spectral element dynamical core in dry-mass vertical coordinates with comprehensive treatment of condensates and energy. *J. Adv. Model. Earth Syst.* **10**, 1537–1570 (2018).

58. R. Döscher *et al.*, The EC-Earth3 Earth system model for the Coupled Model Intercomparison Project 6. *Geosci. Model Dev.* **15**, 2973–3020 (2022).

59. L. Li *et al.*, The flexible global ocean-atmosphere-land system model grid-point version 3 (fgoals-g3): description and evaluation. *J. Adv. Model. Earth Syst.* **12**, e2019MS002012 (2020).

60. J. Dunne *et al.*, The GFDL Earth System Model Version 4.1 (GFDL-ESM 4.1): Overall coupled model description and simulation characteristics. *J. Adv. Model. Earth Syst.* **12**, e2019MS002015 (2020).

61. E. Volodin *et al.*, Simulation of the modern climate using the INM-CM48 climate model. *Russian J. Numer. Anal. Math. Model.* **33**, 367–374 (2018).

62. E. Volodin *et al.*, Simulation of the present-day climate with the climate model INMCM5. *Clim. Dyn.* **49**, 3715–3734 (2017).

63. O. Boucher *et al.*, Presentation and evaluation of the IPSL-CM6A-LR climate model. *J. Adv. Model. Earth Syst.* **12**, e2019MS002010 (2020).

64. A. Sellar *et al.*, UKESM1: Description and evaluation of the UK Earth System Model. *J. Adv. Model. Earth Syst.* **11**, 4513–4558 (2019).

65. F. Nelson, S. Outcalt, A computational method for prediction and regionalization of permafrost. *Arct. Alp. Res.* **19**, 279–88 (1987).